

Improving O₂ production of WO₃ photoanodes with IrO₂ in acidic aqueous electrolyte†

Cite this: *Phys. Chem. Chem. Phys.*,
2014, 16, 3623

Joshua M. Spurgeon,* Jesus M. Velazquez and Matthew T. McDowell

WO₃ is a promising candidate for a photoanode material in an acidic electrolyte, in which it is more stable than most metal oxides, but kinetic limitations combined with the large driving force available in the WO₃ valence band for water oxidation make competing reactions such as the oxidation of the acid counterion a more favorable reaction. The incorporation of an oxygen evolving catalyst (OEC) on the WO₃ surface can improve the kinetics for water oxidation and increase the branching ratio for O₂ production. Ir-based OECs were attached to WO₃ photoanodes by a variety of methods including sintering from metal salts, sputtering, drop-casting of particles, and electrodeposition to analyze how attachment strategies can affect photoelectrochemical oxygen production at WO₃ photoanodes in 1 M H₂SO₄. High surface coverage of catalyst on the semiconductor was necessary to ensure that most minority-carrier holes contributed to water oxidation through an active catalyst site rather than a side-reaction through the WO₃/electrolyte interface. Sputtering of IrO₂ layers on WO₃ did not detrimentally affect the energy-conversion behavior of the photoanode and improved the O₂ yield at 1.2 V vs. RHE from ~0% for bare WO₃ to 50–70% for a thin, optically transparent catalyst layer to nearly 100% for thick, opaque catalyst layers. Measurements with a fast one-electron redox couple indicated ohmic behavior at the IrO₂/WO₃ junction, which provided a shunt pathway for electrocatalytic IrO₂ behavior with the WO₃ photoanode under reverse bias. Although other OECs were tested, only IrO₂ displayed extended stability under the anodic operating conditions in acid as determined by XPS.

Received 31st December 2013,
Accepted 10th January 2014

DOI: 10.1039/c3cp55527e

www.rsc.org/pccp

Introduction

One promising approach to overcome the intermittency of the solar resource and enable widespread use of solar energy is to store it as an energy-dense fuel derived from the photoelectrolysis of water.^{1–3} Perhaps the most efficient way to generate the necessary photovoltage of >1.5 V (thermodynamic voltage plus catalytic overpotentials) while making use of the majority of the solar spectrum is to utilize a tandem cell configuration.^{4,5} In a photoelectrochemical cell without significant corrosion-preventing barrier layers, this scheme requires a reductively stable photocathode and an oxidatively stable photoanode of complementary band gaps.

In theory, such a system could run at any pH, but a cell at neutral pH conditions must deal with the overpotential losses associated with local pH changes at the active sites as well as the eventual formation of a bulk pH gradient, even in the presence of buffer solutions.⁶ These overpotential losses are

mitigated at more extreme pH conditions. Operation in a strongly basic electrolyte is desirable for the increased activity of earth-abundant catalysts at high pH,⁷ but current options are limited for alkaline-stable light absorbers with favorable band gaps and conductive, stable alkaline ion exchange membranes.^{8,9} At low pH, Si,¹⁰ InP,¹¹ and WSe₂¹² are promising reductively stable photocathodes and Nafion, a conductive proton exchange membrane, can meet the operational criteria for a successful product separator in a water-splitting system.¹³ However, there are relatively few candidate materials for an acid-stable photoanode with an appropriate band gap.

Tungsten trioxide, WO₃, an earth-abundant, oxidatively stable semiconductor, is one such material that could fulfill the role of photoanode.^{14–24} In most deposition methods, the presence of oxygen vacancies serve as shallow electron donors and naturally dope the WO₃ n-type.²⁵ Its band gap of 2.6 eV is higher than ideal for the large band gap absorber in a tandem cell. However, N substitution of O atoms in the lattice has been demonstrated to reduce the band gap to as low as 1.9 eV by the addition of N 2p states above the WO₃ valence band, although significant work still remains to achieve a corresponding improvement in stable photocurrent.^{26–29}

Unlike most metal oxides, WO₃ is thermodynamically stable in acidic electrolyte (pH < 4). At higher pH, OH[–] ions induce

Joint Center for Artificial Photosynthesis, California Institute of Technology,
Division of Chemistry and Chemical Engineering, 1200 E. California Blvd. m/c 132-80,
Pasadena, CA 91125, USA. E-mail: spurgeon@caltech.edu

† Electronic supplementary information (ESI) available. See DOI: 10.1039/c3cp55527e

chemical dissolution by the reaction $\text{WO}_3(\text{s}) + \text{OH}^- \rightarrow \text{WO}_4^{2-} + \text{H}^+$.^{30,31} Even in acidic conditions, some photocorrosion of WO_3 has been observed due to the formation of peroxy-species as intermediates during water oxidation.^{22–24,32} Although peroxide formation and the oxidation of most acid counterion species are reactions that are thermodynamically less feasible than water oxidation, the kinetics of these reactions are often more favorable than oxygen evolution.¹⁴ The photogenerated minority-carrier holes in the valence band of WO_3 have a potential of ~ 2.97 V vs. NHE at pH 0.³³ This potential is sufficient to drive many competing reactions, thus limiting the faradaic oxygen evolution efficiency on bare WO_3 . Researchers have demonstrated enhanced photostability of WO_3 near neutral pH by annealing in a hydrogen environment³⁴ and by adding thick coatings of an oxygen evolution catalyst (OEC) to reduce the required oxygen evolution overpotential and kinetically favor water oxidation over peroxy-species formation.²¹

The selectivity for water oxidation of WO_3 photoanodes without a co-catalyst depends strongly on the electrolyte species and pH. No O_2 formation is observed in HCl or acetic acid solutions and O_2 yields decrease with decreasing pH in H_3PO_4 and H_2SO_4 .¹⁴ In strongly acidic media, the photocurrent that does not contribute to water oxidation or peroxy-species formation has been ascribed mainly to oxidation of the acid counterion (*i.e.*, the conversion of 2Cl^- to Cl_2 in HCl or of 2SO_4^{2-} to $\text{S}_2\text{O}_8^{2-}$ in H_2SO_4).³⁵

To our knowledge, the effects of OECs on the branching ratio for O_2 production relative to SO_4^{2-} oxidation on WO_3 in H_2SO_4 has not been investigated. Furthermore, since the catalyst deposition method is known to have a significant impact on the charge-transfer in other semiconductor photoelectrodes, its effect on WO_3 is of considerable interest. In the work reported here, we investigate the faradaic oxygen production efficiency for IrO_2 on WO_3 in acid and explore the effect of the method of catalyst attachment on the photoelectrochemical energy-conversion behavior.

Experimental

WO_3 electrode fabrication

Thin films of WO_3 were fabricated on fluorine-doped tin oxide (FTO, TEC 15) coated glass substrates (Hartford Glass Company Inc.) by an RF sputtering method.³⁶ A W metal target (Lesker, 99.95%) was used in an AJA International sputtering system at 200 W on an RF source for 2 h at 200 °C under a constant flow of 16.0 sccm Ar and 4.0 sccm O_2 while maintaining an overall pressure of 10 mTorr. Part of the FTO glass slide was masked off during sputtering for later contacting during electrode fabrication. After sputtering, the WO_3 thin films were then annealed at 400 °C in air for 2 h to improve the crystallinity. Catalysts were then deposited by various methods (see below), and the sample was made into an electrode by contacting a Cu wire to the exposed FTO with Ag paint, then putting the wire in a glass tube and sealing the exposed wire and FTO surfaces in epoxy. The exposed area of catalyst/ WO_3 was $\sim 1 \text{ cm}^2$ in all

cases, with the same area exposed on either side of the glass slide to enable either front or back illumination. WO_3 on W foil electrodes were fabricated in an identical fashion, substituting W foil (Alfa Aesar) for FTO/glass and completely encasing the back of the electrode in epoxy since back illumination through the metal foil was not possible.

Catalyst deposition

For the spin-coated, sintered catalyst electrodes, IrO_2 was deposited onto thin WO_3 films by spin-casting a metal salt solution and then sintering to achieve the oxide form.³⁷ An iridium chloride ($\text{IrCl}_3 \cdot x\text{H}_2\text{O}$, 99.9%, Strem Chemicals) solution at 0.025 M in ethanol with 0.15 g of Triton X-100 surfactant per mmol of Ir was drop-cast on a cleaned FTO glass slide then spun at 5000 rpm for 90 s. The film was sintered to IrO_2 by annealing in air at 400 °C for 30 min. For electrodes with 2 coats of spin-coated IrO_2 , the process was repeated a second time. Analogous electrodes of IrO_2 directly on FTO glass were produced by the same method. Photoelectrodes using a simple approach to drop-cast and sinter catalyst from solution on WO_3 were tested as well (see ESI†).

For the sputtered catalyst electrodes, IrO_2 films were sputtered from an Ir metal target ($\geq 99.9\%$ from ACI Alloys, Inc.). The catalyst layer was sputtered onto the WO_3 film from an RF source at 200 W at 300 °C under a constant flow of 3.0/3.0 sccm Ar/O_2 while maintaining an overall pressure of 5 mTorr. Two different thicknesses of catalyst were produced by sputtering for either 0.5 min ($< 10 \text{ nm}$) or 30 min ($> 100 \text{ nm}$). Analogous electrodes of IrO_2 directly on FTO glass were produced by the same method.

For electrodeposited catalyst electrodes, a literature method was used to electrodeposit IrO_2 .³⁸ An aqueous electrodeposition bath of 20 mM oxalic acid and 4 mM K_3IrCl_6 was adjusted to pH 10 with Na_2CO_3 and aged for > 10 days.³⁸ IrO_2 was then anodically electrodeposited (with a Ag/AgCl reference and a fritted Pt gauze counter electrode) onto $\sim 1 \text{ cm}^2$ of WO_3 on FTO at 0.85 V vs. Ag/AgCl until 400 mC of charge had passed. The potential was selected to provide $\sim 300 \mu\text{A cm}^{-2}$ on FTO, the same current density as the published method. Both as-deposited and annealed (400 °C for 1 h in air) electrodes were tested. Analogous electrodes of IrO_2 electrodeposited directly on FTO glass were produced by the same method. A second IrO_2 electrodeposition procedure was tried as well (see ESI†).³⁹

Drop-cast particulate IrO_2 on WO_3 was also fabricated and tested (see ESI†).

Photoelectrochemical $J-E$ measurements

Current density vs. potential ($J-E$) photoelectrochemical energy-conversion behavior for all electrodes was measured in 1 M H_2SO_4 (made with 18 MΩ cm H_2O) under stirring with the FTO/glass slide as working electrode, a Pt gauze counter electrode separated from the main cell compartment by a glass frit, and a Ag/AgCl, KCl (saturated) reference electrode (CH Instruments, Inc.) in a glass cell with a flat quartz window for illumination. The potential was scanned at 30 mV s^{-1} between 0.2 and 2.0 V vs. Ag/AgCl and the data collected using a Bio-Logic SP-200

potentiostat. The data reported herein is for the second scan on each electrode. Electrochemical measurements were referred to the reversible hydrogen electrode (RHE) by the equation: $V_{\text{RHE}} = V_{\text{Ag}/\text{AgCl}} + 0.197 + \text{pH}(0.059)$, with the pH for 1 M H₂SO₄ = 0. Simulated sunlight at an intensity of 100 mW cm⁻² at normal incidence to the working electrode was generated with a 150 W Xe lamp (Newport 6255) coupled with an AM1.5 global filter (Newport 81094) and calibrated in the electrolyte with a Si photodiode (Thorlabs FDS100-CAL). Under front illumination, the light was incident on the catalyst layer, while under back illumination the light passed through the transparent substrate to the WO₃ without passing through the catalyst layer (Fig. S1, ESI†).

O₂ measurements

The O₂ concentration was measured in the electrochemical cell using a fluorescence-based oxygen sensor (NeoFox, Ocean Optics) with the optical fiber inside a sealed glass tube inserted into the electrolyte with an O₂-sensitive fluorescent patch (HIOXY, Ocean Optics) on the outside of the glass tube. The oxygen sensor was calibrated against an air-saturated solution of 1.0 M H₂SO₄(aq), using an O₂ solubility of 7.7 mg L⁻¹ under 0.21 atm of O₂(g) partial pressure.⁴⁰ The cell electrodes (catalyst/ WO₃ working, fritted Pt gauze counter, Ag/AgCl reference) and oxygen sensor were sealed tightly using thermometer adapters (Ace Glass) and the cell was completely filled with electrolyte to avoid any headspace volume. Before measurement, the electrolyte was purged with UHP Ar(g) for >30 min. During measurement, the working electrode was kept at open-circuit potential for 10 min, then maintained at the water oxidation potential (1.2 V vs. RHE) for 30 min, and then again held at open-circuit potential for another 10 min, with the cell under illumination and stirred vigorously. The illumination intensity was adjusted to provide sufficient current without any noticeable bubble formation (generally <1.5 mA cm⁻²). To minimize noise and drift in the oxygen sensor measurement, the fluorescent patch was blocked from the path of the incident illumination and an infrared water filter (Newport 61945) was used in conjunction with the Xe lamp to minimize heating in the electrolyte. The ambient O₂(g) leak rate into the cell was established by analyzing the response during the periods at open-circuit and subtracting it from the total response. Faradaic oxygen production efficiency, η_{O_2} , was estimated by comparing the measured O₂ output after 30 min of oxidation to the accumulated charge passed assuming 100% O₂ yield.

Fast one-electron redox couple measurements

WO₃ on W foil electrodes were used for measurements in a ferro-/ferricyanide electrolyte. A Pt mesh counterelectrode (without a frit) and a Pt wire reference poised at the solution potential were used in a 0.35 M K₄Fe(CN)₆–0.05 M K₃Fe(CN)₆(aq) (99%, Sigma-Aldrich) solution under vigorous stirring.

X-ray photoelectron spectroscopy (XPS)

All spectra were collected on a Kratos Axis Ultra system (base pressure 10⁻⁹ Torr), with a monochromated Al K α X-ray source at a power of 150 W. A pass energy of 80 eV was used for survey scans and 10 eV for all high resolution spectra. Photoelectrons

were collected at surface normal with a hemispherical analyzer. The photoemission energy scale was calibrated to the adventitious C 1s peak (set to 284.8 eV) measured for each sample. All peaks were fit using Casa XPS software with a Shirley background and symmetric Voigt lineshapes that were 70% Gaussian and 30% Lorentzian product functions.

Electron microscopy

Scanning electron microscopy (SEM) images were taken on a Nova NanoSEM 450 (FEI, Hillsboro, OR). High-resolution transmission electron microscopy (HRTEM) was performed with a Tecnai F30ST system (FEI, Hillsboro, OR) at a voltage of 300 kV. To prepare IrO₂/WO₃/FTO/glass cross-sections for HRTEM and selected-area electron diffraction (SAED), the excess glass was cut and polished to ~100 μm and further thinned using a dimpler and then ion mill to reach a thickness of ~100 nm. The cross-sectioned samples were then mounted onto 50 μm single slot Ni grids for imaging.

Results and discussion

IrO₂ on WO₃ contact with fast, one-electron redox couple

A fast, one-electron redox couple that can transfer charge with the electrode without significant kinetic limitations is a useful diagnostic tool to investigate the IrO₂/WO₃ contact. The ferro-/ferricyanide (Fe(CN)₆^{4-/-3-}) redox couple was used for this purpose. Without the kinetic limitations of water oxidation, pathways allowing the electrolyte to encounter the back contact would result in shunts that can dominate the J - E behavior. To prevent shunting, WO₃ was deposited on W foil substrates and subsequently annealed in air to ensure that only WO₃ was exposed to solution. For water oxidation studies in aqueous sulfuric acid, FTO/glass substrates were used instead to enable back illumination. In 1 M H₂SO₄ under front illumination, WO₃/W foil photoanodes produced similar photoelectrochemical performance to WO₃ on FTO/glass (Fig. S2a, ESI†).

Fig. 1 shows the dark electrochemical behavior of these electrodes in the ferro-/ferricyanide solution. Bare W foil displayed characteristic ohmic behavior, reaching limiting anodic

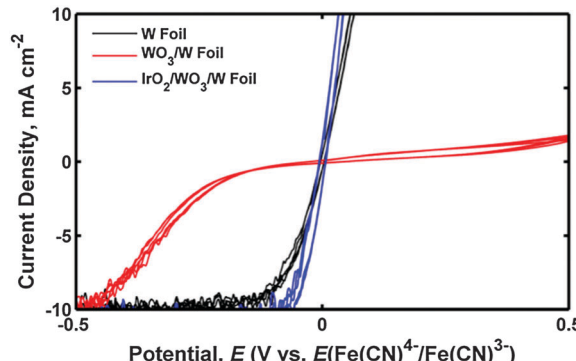


Fig. 1 Electrochemical behavior in ferro-/ferricyanide. Current-density (J) vs. potential (E) behavior in 0.35 M K₄Fe(CN)₆–0.05 M K₃Fe(CN)₆(aq) for (black line) bare W foil, (red line) WO₃ on W foil, and (blue line), 30 min sputtered IrO₂ on WO₃ on W foil.

and cathodic currents resulting from mass transport limitations of the redox species to the electrode surface.⁴¹ Annealed WO_3 on W foil, however, resulted in diodic $J-E$ behavior indicative of a semiconductor supporting a built-in electric field due to Fermi level equilibration with the redox species. This behavior demonstrated the lack of shunting in the WO_3/W foil electrodes.

Upon sputtering a thick IrO_2 layer on a WO_3/W foil electrode (while carefully masking the IrO_2 to ensure deposition only on the WO_3 and to avoid edge effects), the electrochemical response in ferro-/ferricyanide reverted to behavior characteristic of an ohmic contact. This data suggests the junction between the IrO_2 catalyst and the WO_3 photoanode is quite ohmic. With a conformal, compact IrO_2 layer, the IrO_2/WO_3 interface would be predicted to control the junction and produce little photocurrent. Likewise, a low energy barrier between the catalyst and semiconductor implies that the IrO_2 can shunt through the WO_3 to the back contact, which makes electrocatalytic current at higher potentials possible even though the photodiode should be in reverse bias (Fig. S2b, ESI†). Similar behavior has been reported for IrO_x on other metal oxide photoanodes.⁴² Direct solid-state contact measurements of IrO_2 on WO_3 also suggested ohmic behavior (Fig. S3, ESI†).

Sintered IrO_2 on WO_3 photoanodes

A simple method for uniform heterogeneous catalyst attachment is to spin-coat solutions of metal salts onto the electrode and then sinter them.³⁷ Sintering produced the catalytically active metal oxide form of the OEC adhered to the semiconductor surface. IrO_2 , although not earth-abundant, was the primary catalyst of interest in this study owing to its known high activity for water oxidation and stability in acid. Co_3O_4 and RuO_2 were also initially investigated with some attachment methods (see ESI†) but neither is stable in strongly acidic media.⁴³

Fig. 2 shows the photoelectrochemical current-density vs. potential ($J-E$) behavior for a spin-coated, sintered IrO_2 on WO_3 photoanode as compared to bare WO_3 or sintered IrO_2 on the FTO/glass. While higher photocurrents from bare sputtered WO_3 films have been reported (although with significant reproducibility issues attributed to such factors as choice of W sputter target),⁴⁴ the effect of catalyst attachment, rather than maximized photocurrent, was the main purpose of this study. The WO_3 photoelectrochemical behavior observed herein is consistent with results reported by other groups in sulfuric acid electrolyte.^{14,35} For one layer of spin-coated, sintered IrO_2 (~1 nm thick) on WO_3 (Fig. 2a), the back-illuminated photocurrent at 1.5 V vs. RHE was comparable to that for bare WO_3 ; however, under front illumination the photocurrent was reduced due to parasitic light absorption in the catalyst layer (Fig. S9, ESI†).⁴⁵ At >1.5 V, the current increased exponentially which indicated the presence of a shunt allowing the electrocatalytic response of IrO_2 to dominate, consistent with the observations using a fast, one-electron redox couple. Additionally, the open-circuit potential shifted from 0.53 V to 0.65 V vs. RHE upon the attachment of the sintered catalyst layer, a 120 mV reduction in photovoltage. The decrease in the open circuit voltage and photocurrent shows that the spin coating and

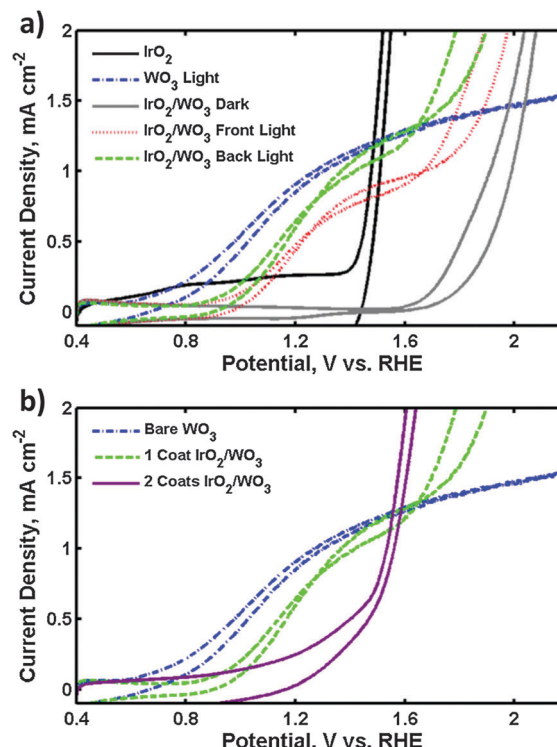


Fig. 2 $J-E$ behavior for sintered IrO_2 on WO_3 . Photoelectrochemical current-density (J) vs. potential (E) behavior in 1 M H_2SO_4 for IrO_2 sintered from spin-coated IrCl_3 solutions on WO_3 thin films. Performance is shown for (a) one coating of IrO_2 under (green lines) back illumination, (red lines) front illumination, and (gray lines) in the dark, with (blue lines) bare WO_3 under illumination and (black lines) the catalyst by itself in the dark for reference. Also shown is (b) the effect of catalyst thickness by comparing (blue lines) bare WO_3 to (green lines) one coat of IrO_2 to (purple lines) two coats of IrO_2 , all under back illumination.

annealing of IrO_2 on WO_3 degraded the photoelectrochemical junction compared to pure WO_3 .

Despite the decreased $J-E$ performance, these electrodes increased the O_2 yield from 0% for bare WO_3 to 82% for one coat of sintered IrO_2 (Table 1). Hence, although the sintered IrO_2 layer had an adverse impact on the photoelectrochemical junction, the active catalytic sites increased the branching ratio for water oxidation relative to sulfate oxidation.

A second layer of spin-coated, sintered IrO_2 (Fig. 2b) further degraded the photoelectrochemical response, reducing the photocurrent significantly. This reduction occurred under both front and back illumination, indicating that changes to the junction, rather than parasitic catalyst light absorption, account for the decreased performance. Much thicker sintered IrO_2 on WO_3 photoanodes, fabricated by drop-casting the catalyst layer rather than spin-coating, were observed to be photo-inactive (Fig. S5, ESI†). These observations are consistent with the explanation that as the sintered catalyst layer becomes thicker and more contiguous, the junction is increasingly dominated by the IrO_2/WO_3 interface rather than the $\text{WO}_3/\text{liquid electrolyte}$, leading to a significant reduction in the barrier height and resultant photoresponse.

Table 1 Effect of catalyst attachment method on current density and oxygen yield

IrO ₂ deposition method	J_{back}^a	J_{front}^b	$\eta_{\text{O}_2}^c$
None, bare WO ₃	0.93 ^d	0.91	0
Sintering, spin-coated (1 coat)	0.71	0.53	82
Sintering, spin-coated (2 coats)	0.17	0.11	—
Sintering, drop-cast	0.01	0.01	—
Sputtering, 0.5 min	0.91	0.53	68
Sputtering, 30 min	0.90	0.03	99
Drop-cast particles ^e	0.95	0.30	0
Drop-cast particles, annealed ^e	0.54	0.17	43
Electrodeposition	0.95	0.49	—
Electrodeposition, annealed	0.25	0.25	—

^a Current density in mA cm⁻² under 100 mW cm⁻² AM1.5 back illumination at 1.2 V vs. RHE. ^b Current density in mA cm⁻² under 100 mW cm⁻² AM1.5 front illumination at 1.2 V vs. RHE. ^c Faradaic O₂ efficiency (%) over 30 min under illumination at 1.2 V vs. RHE. O₂ yield was not measured for electrodes that exhibited significantly reduced photocurrent relative to bare WO₃, or for electrodeposited IrO_x due to the observed instability in acid. ^d Current density for bare WO₃ exhibited a variability of ± 0.10 mA cm⁻². ^e Details on drop-casting IrO₂ particles are in the ESI.

Sputtered IrO₂ on WO₃ photoanodes

Reactive sputtering of a metal target in the presence of an oxygen partial pressure allows the deposition of a thin film of a metal oxide without a post-processing annealing step. This catalyst attachment method provides a high surface coverage in which the metal oxide can be controllably deposited in a thin enough layer to enable a high optical transparency. Thin films (<10 nm) of IrO₂ were deposited onto WO₃ photoanodes by sputtering for 0.5 min, and thick films (>100 nm) were analogously made by sputtering for 30 min. XPS spectra of the resulting sputtered films confirmed the presence of the expected IrO₂ composition (Fig. S6, ESI†). These two extremes of thickness ensured that in one system a significant amount of light would pass through the catalyst layer during front illumination while the other provided the ideal catalysis achievable with a sputtered film.

Fig. 3 shows the J - E behavior for sputtered IrO₂/WO₃ photoanodes. Unlike the behavior with sintered catalyst layers, even for thick sputtered IrO₂ layers the performance under back illumination was comparable to the photocurrent achieved with bare WO₃ (Table 1), demonstrating that sputtered IrO₂ did not detrimentally affect the photoelectrochemical junction of the photoanode. Even a thin sputtered catalyst layer, however, caused significant parasitic light absorption as evidenced by the reduced photocurrent during front illumination. 30 min sputtered IrO₂ layers were optically opaque at this thickness, and the photoelectrodes yielded essentially no photocurrent when illuminated from the front side. Again, onset of the electrocatalytic wave at >1.4 V vs. RHE when the photoanode is in reverse bias was indicative of a shunt to the catalyst. Annealing the sputtered IrO₂/WO₃ photoanodes at 400 °C in air under the same conditions used for sintered IrO₂ did not significantly affect the photoelectrochemical performance (Fig. S10, ESI†).

Fig. 4 shows the variation in morphology of IrO₂ layers. The top-down SEM images showed that sintered IrO₂ layers on WO₃

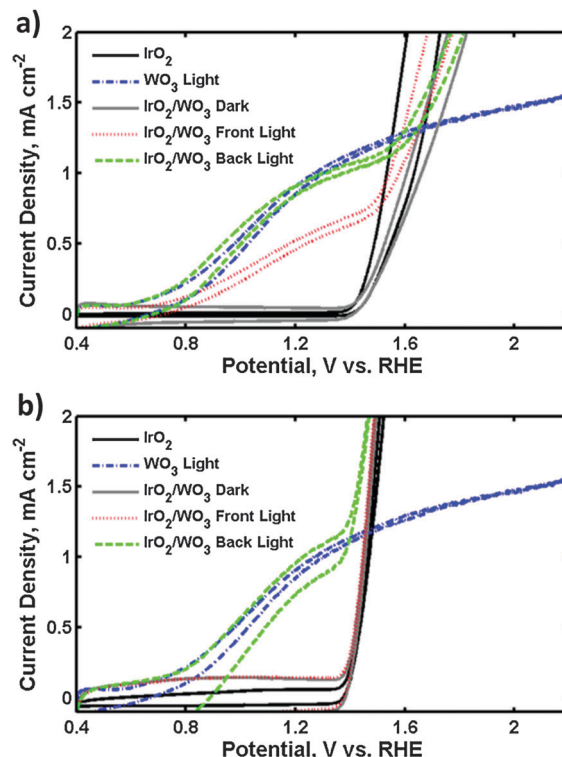


Fig. 3 J - E behavior for sputtered IrO₂ on WO₃. Photoelectrochemical current-density (J) vs. potential (E) behavior in 1 M H₂SO₄ for a (a) thin, 0.5 min sputtered IrO₂ film and a (b) thick, 30 min sputtered IrO₂ film on WO₃. Performance is shown for (green lines) back illumination, (red lines) front illumination, and (gray lines) in the dark, with (blue lines) bare WO₃ under illumination and (black lines) the catalyst by itself in the dark for reference.

were more contiguous and compact as compared to the bare WO₃ (Fig. 4a) surface as the catalyst layer became thicker from spin-coated (Fig. 4b) to drop-cast (Fig. 4c) IrO₂. Thick, sputtered IrO₂ films consisted of catalyst platelets on the order of ~ 100 nm (Fig. 4d). However, TEM results for sputtered IrO₂/WO₃ electrodes demonstrated the polycrystalline nature of the sputtered deposit, with grain sizes of ~ 1 nm (Fig. 4g and Fig. S11, ESI†). This difference in catalyst layer morphology may be a possible explanation for the observed differences in photoelectrochemical behavior between sintered and sputtered IrO₂ layers on WO₃ photoanodes. As a more compact film, even a thin, conformal layer of sintered IrO₂ (Fig. 4e and f) may be enough to interfere with the interfacial energetics of the system and ensure that the IrO₂/WO₃ contact dominates the junction rather than the WO₃/solution junction. The sputtered films on WO₃, however, appear more porous (Fig. 4h). This porosity may enable the electrolyte to permeate through the catalyst layer to the WO₃ surface and into the nanoporous bulk of the WO₃. The liquid electrolyte/WO₃ interface then gives rise to band bending and J - E performance comparable to bare WO₃ despite >100 nm of sputtered IrO₂ at the surface.

Previous work has established that WO₃ photocurrent in highly acidic electrolyte is not necessarily due to the oxidation of water, and in H₂SO₄ most of this current results in the oxidation of SO₄²⁻ to S₂O₈²⁻.^{14,35} Thus the faradaic efficiency

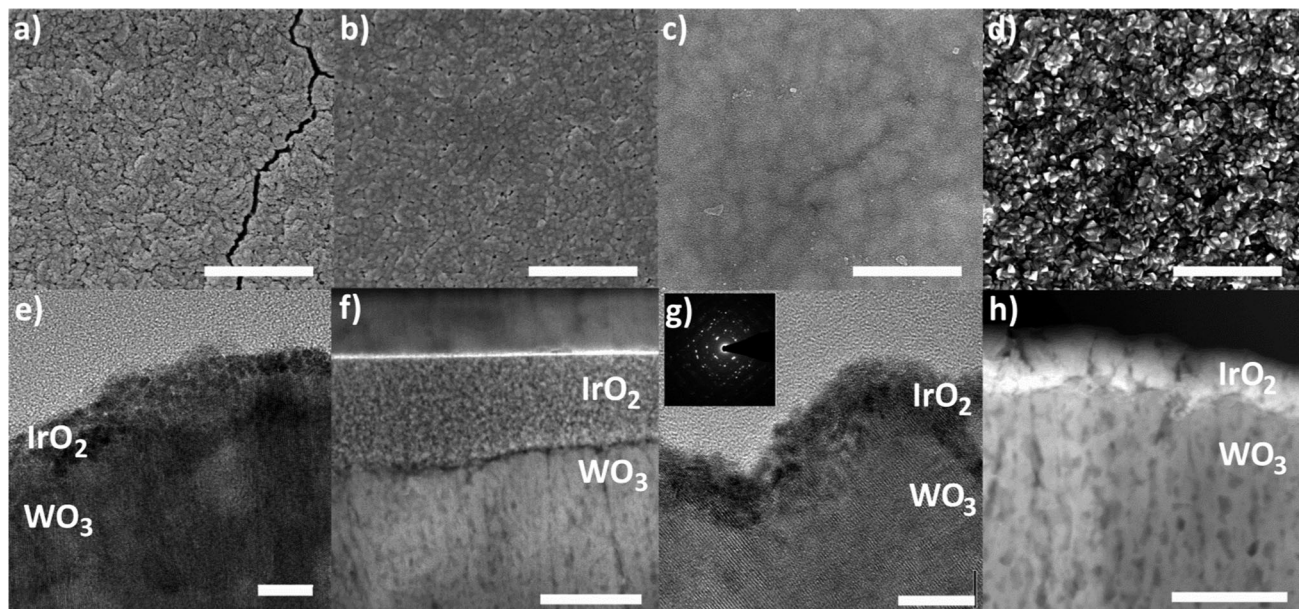


Fig. 4 Morphology of IrO_2 on WO_3 . (a–d) Top-view SEM images of (a) bare WO_3 , (b) spin-coated, sintered IrO_2/WO_3 , (c) drop-cast, sintered IrO_2/WO_3 , and (d) thick, sputtered IrO_2/WO_3 . The scale bar in (a–d) is 1 μm . (e, g) Cross-sectional TEM images and (f, h) cross-sectional scanning TEM-high angle annular dark field (TEM-HAADF) images of (e) spin-coated, sintered IrO_2/WO_3 , (f) drop-cast, sintered IrO_2/WO_3 , (g) thin, sputtered IrO_2/WO_3 with (g inset) electron diffraction pattern confirming polycrystallinity in the sputtered IrO_2 layer, and (h) thick, sputtered IrO_2/WO_3 . The scale bar in (e, g) is 10 nm and in (f, h) is 200 nm.

for O_2 production for these photoanodes was directly measured to determine the efficacy of each OEC attachment strategy. A fluorescence-based oxygen sensor (see Experimental) was employed to unambiguously separate water oxidation from sulfate oxidation. The O_2 yield of bare WO_3 in 1 M H_2SO_4 was established by measuring O_2 production under potentiostatic conditions at different applied biases (Fig. S12, ESI†). WO_3 by itself was observed to have a faradaic oxygen production yield, η_{O_2} , of 29% at 2.0 V vs. RHE, decreasing to ~0% below 1.4 V vs. RHE. To be useful for photoelectrochemical water-splitting, the photoanode needs to produce O_2 from H_2O in its power-producing region, below the water oxidation potential (<1.23 V vs. RHE) with high faradaic efficiency.

Fig. 5 shows O_2 production measurements for WO_3 photoanodes with both thin and thick sputtered IrO_2 layers biased at 1.2 V vs. RHE. Sputtered IrO_2 by itself was measured as well (at higher bias to produce the necessary current) to demonstrate the near unity O_2 yield achievable with IrO_2 . Thicker sputtered IrO_2 films on WO_3 increased the η_{O_2} to ~100% O_2 yield compared to 68% for thin layers (Table 1). However, in a tandem water-splitting cell the wide band gap electrode needs to be the initial or top light absorber. Thus, in an integrated tandem configuration, WO_3 would be the top cell and be illuminated from the front side. Therefore, a tradeoff exists between high water oxidation rates that are favored by high catalyst loadings and low parasitic light absorption that favors low catalyst loadings. The optimal catalyst thickness would maximize the front illuminated oxygen production rate.

To be an effective photoanode, the catalyst and light absorber combination must be stable under oxidative conditions in the

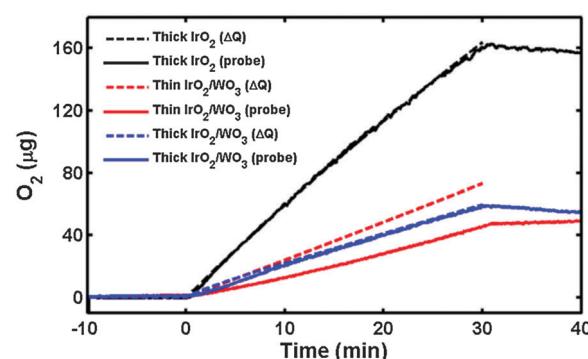


Fig. 5 O_2 production of sputtered IrO_2 on WO_3 . The amount of O_2 produced at 1.2 V vs. RHE under back illumination in 1 M H_2SO_4 for a WO_3 photoanode with a sputtered IrO_2 catalyst layer. The quantity of O_2 was determined by (dashed lines, ΔQ) the total charge passed (assuming 100% faradaic conversion to O_2) and by (solid lines, probe) an optical O_2 sensor. For catalyst thickness, (red lines) a thin film was sputtered for 0.5 min, and (blue lines) a thick film was sputtered for 30 min. To demonstrate the high faradaic efficiency achievable with the catalyst, (black lines) bare IrO_2 films were measured in the dark at 1.5 V vs. RHE.

electrolyte. As reported in previous work,¹⁴ the bare WO_3 photocurrent decayed over time; however, in many cases the photocurrent recovered after the measurement of a cyclic voltammogram (Fig. S15a, ESI†). Even after photocurrent decay from >60 h under operation, rinsing the electrode and measuring in fresh electrolyte recovered much of the photocurrent and resulted in $J-E$ behavior similar to the original performance.

XPS spectra of the relevant peaks were examined for changes after $J-E$ measurement and after an extended stability test in

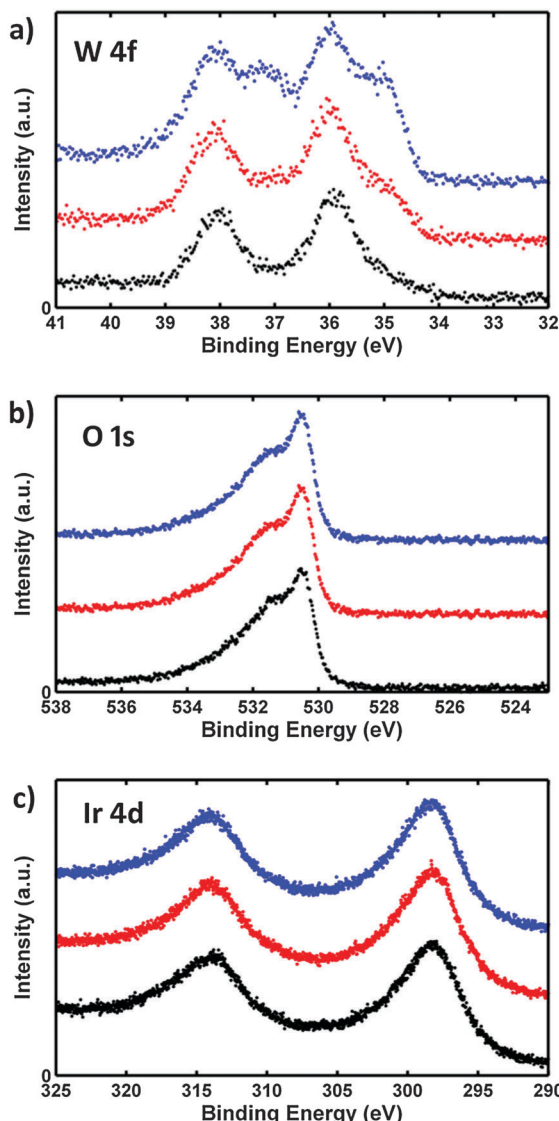


Fig. 6 XPS of sputtered IrO_2 on WO_3 . High resolution XPS spectra for WO_3 films covered with thin, sputtered IrO_2 . The regions shown are (a) W 4f, (b) O 1s, and (c) Ir 4d. The films were analyzed (black lines) as-deposited, (red lines) after a J - E behavior measurement under illumination in 1 M H_2SO_4 , and (blue lines) after 12 h at 1.2 V vs. RHE under illumination in 1 M H_2SO_4 .

which the electrode was biased at 1.2 V vs. RHE under illumination for 12 h. For bare WO_3 , neither the W nor the O peaks showed any noticeable difference after the extended stability test (Fig. S15b and c, ESI†). Fig. 6 shows the XPS spectra for thin, 0.5 min sputtered IrO_2/WO_3 electrodes in which the catalyst layer was thin enough to allow sampling of the underlying WO_3 . Of the OECs tested, only IrO_2 was stable in 1 M H_2SO_4 for a significant time (see ESI†), with no noticeable change in the O 1s or Ir 4d regions even after the extend stability test (Fig. 6b and c). Interestingly, the IrO_2/WO_3 W 4f region did change, with a doublet peak rising at 35.0 eV (Fig. S16, ESI†). Based on NIST XPS peak assignments for tungsten species, we tentatively assign this to either H_2WO_4 that could arise from a reaction with a peroxy species, or perhaps even an iridium tungstate species at the interface. The robustness of the thin

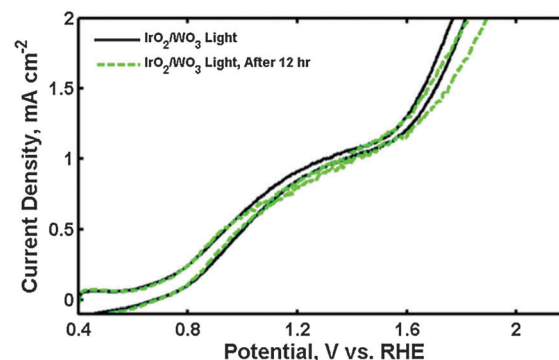


Fig. 7 Stability of sputtered IrO_2 on WO_3 . Photoelectrochemical current-density (J) vs. potential (E) behavior in 1 M H_2SO_4 under back illumination for a 0.5 min sputtered film of IrO_2 on WO_3 (black line) as-deposited, and (green line) after 12 h at 1.2 V vs. RHE in 1 M H_2SO_4 under illumination when rinsed and measured in fresh electrolyte.

sputtered IrO_2 on WO_3 is further demonstrated in Fig. 7, in which the photoanode, after an extended stability test, was rinsed and put in a fresh 1 M H_2SO_4 electrolyte to measure the J - E behavior. Changes in the shape of the curve were minimal, and even after 12 h under operation, the catalytic onset current beyond 1.4 V vs. RHE remained.

Electrodeposited IrO_x on WO_3 photoanodes

Electrodeposition of the IrO_2 layer was also investigated as a catalyst attachment method capable of high surface coverage. Previous studies have shown that electrodeposited catalysts can be effective at improving the performance of photoanodes.^{21,46} An established literature method for electrodepositing IrO_x on FTO was used in this work.³⁸ The electrodeposition proceeded until 400 mC of charge had passed with a 1 cm^2 substrate, providing the same catalyst loading for each sample.

The resulting J - E behavior for IrO_x on FTO showed high catalytic current at >1.4 V vs. RHE as expected, but with a slight decay during successive scans (Fig. 8a). Electrodeposited IrO_x/WO_3 electrodes, however, displayed complex behavior with significant hysteresis between the forward and reverse scans as well as large redox peaks around 0.8 V vs. RHE. This general behavior has been observed before for electrodeposited IrO_x on a metal oxide photoanode,⁴² with the peaks at 0.8 V vs. RHE ascribed to an $\text{Ir}(\text{III})/\text{Ir}(\text{IV})$ redox process with a large capacitance that leads to the hysteresis.^{47,48} The averaged photocurrent under back illumination agreed well with bare WO_3 (Table 1); however, the catalytic current was unstable and decayed progressively as the samples were measured with back and then front illumination followed by a dark curve.

Evidently, a reaction is proceeding in this instance that was not occurring with IrO_2 deposited by other methods. New electrodeposited IrO_x/WO_3 electrodes were subsequently annealed at 400 °C in air for 1 h to ensure complete oxidation of the catalyst. The current from both electrodeposited IrO_x/WO_3 and IrO_x directly on FTO stabilized due to the anneal, and the redox peaks nearly disappeared (Fig. 8b). This result corroborated previous work on a similar electrodeposited

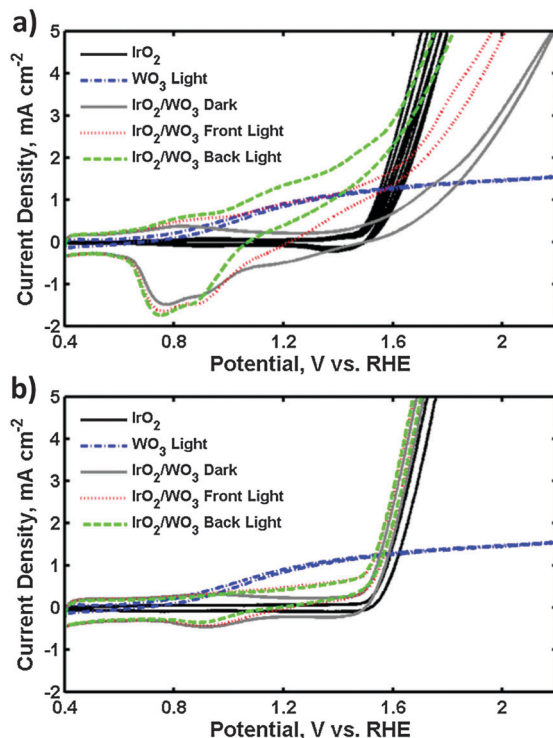


Fig. 8 J - E behavior for electrodeposited IrO_x on WO_3 . Photoelectrochemical current-density (J) vs. potential (E) behavior in 1 M H_2SO_4 for electrodeposited IrO_x on WO_3 (a) as-deposited and (b) after a 400 °C anneal for 1 h. Performance is shown for (green lines) back illumination, (red lines) front illumination, and (gray lines) in the dark, with (blue lines) bare WO_3 under illumination and (black lines) the catalyst by itself in the dark for reference. Multiple successive scans of the catalyst by itself are included to demonstrate unstable current in (a) and stable current in (b).

hydrous $(\text{Ru} + \text{Ir})\text{O}_x$, which was unstable in H_2SO_4 as-deposited but stabilized upon annealing.⁴⁸

During annealing, trapped water is vaporized from the electrodeposited film and the catalyst is fully oxidized, leading to a denser layer.⁴⁸ Unfortunately, after annealing the electrodeposited IrO_2/WO_3 photocurrent declined to approximately one fourth of its as-deposited, back-illuminated value (Table 1), possibly due to the same mechanism that degraded the J - E behavior of sintered IrO_2/WO_3 photoanodes. It is speculated that the hydrous nature of the as-deposited IrO_x films allows the liquid electrolyte/ WO_3 junction to establish band bending, but upon annealing to a denser IrO_2 layer, the IrO_2/WO_3 interface dominates. XPS spectra of the electrodeposited IrO_x on WO_3 electrodes confirm that the catalyst is not primarily in the IrO_2 state until after the annealing step (Fig. S17, ESI†). A second electrodeposition method, which has been shown to yield highly active nanoparticulate IrO_x films on glassy carbon and FTO from a colloidal suspension of IrO_x ,³⁹ resulted in similar behavior to the first electrodeposition method when deposited on WO_3 (Fig. S18, ESI†).

Although electrodeposition is a promising strategy for high coverage, conformal catalyst attachment that has been demonstrated effectively by other groups, it may not work well unless the as-deposited catalyst is in a stable, active form. Annealed,

electrodeposited IrO_x on WO_3 may perform similarly to spin-coated, sintered IrO_2 on WO_3 if it can be deposited uniformly at a comparable thickness (1–2 nm).

Conclusions

WO_3 is a promising photoanode material that is unusual for its stability in acidic media, but its selectivity for water oxidation over side reactions is dependent on the electrolyte and generally very low at low pH. The O_2 yield can be improved with the incorporation of an OEC, but the method of catalyst attachment is critical to determining the performance of the photoanode. The surface coverage of catalyst on the semiconductor must be high enough to promote charge-transfer to a catalytically active site rather than the WO_3 /electrolyte interface where oxidation of the acid counterion is more favorable. Sputtering OEC layers was the most effective attachment strategy tried in this work, with IrO_2 being the most stable catalyst in strong acid. Sputtered IrO_2 on WO_3 greatly increased the faradaic oxygen production efficiency, with nearly complete water oxidation observed for thick catalyst layers; however, a tradeoff exists for sputtered catalysts between high O_2 yield and low parasitic light absorption that must be optimized. Measurements in an electrolyte with a fast, one-electron redox couple indicate that the IrO_2/WO_3 junction is ohmic, which results in poor photoelectrochemical performance when compact, conformal catalyst layers more than a few nm in thickness coat the semiconductor. Good photoelectrochemical performance under back illumination with thick sputtered catalysts is attributed to the porous morphology of these layers.

The results indicate that an ideal OEC layer would be one that is highly conformal yet optically transparent, thin and/or porous enough to allow the liquid electrolyte to control the interfacial energetics, and deposited in a stable, catalytically active form. Atomic layer deposition (ALD) of ultrathin metal oxide catalysts, in which the layer is not thick enough to dominate the photoelectrochemical junction, therefore seems like a promising avenue for future catalyst attachment studies to photoanodes. Alternatively, appropriately spaced catalyst particles small enough to be in the “pinch-off” regime, in which the liquid/semiconductor junction potential would control the energetics even in the regions where catalyst is present,⁴⁹ could also lead to efficient photoanodes with a high O_2 yield. Lastly, it should be acknowledged that Ir is one of the rarest elements on Earth, and unless a low-overpotential, acid-stable OEC other than IrO_2 is identified, highly scalable photoanode systems may require a shift toward higher pH.

Acknowledgements

This material is based upon work performed by the Joint Center for Artificial Photosynthesis, a DOE Energy Innovation Hub, supported through the Office of Science of the U.S. Department of Energy under Award Number DE-SC0004993. XPS data were collected at the Molecular Materials Research Center of the Beckman Institute of the California Institute of Technology.

Notes and references

- Published on 10 January 2014. Downloaded by California Institute of Technology on 13/03/2014 14:40:41.
- 1 N. S. Lewis and D. G. Nocera, *Proc. Natl. Acad. Sci. U. S. A.*, 2006, **103**, 15729–15735.
 - 2 M. Gratzel, *Acc. Chem. Res.*, 1981, **14**, 376–384.
 - 3 A. J. Bard and M. A. Fox, *Acc. Chem. Res.*, 1995, **28**, 141–145.
 - 4 M. G. Walter, E. L. Warren, J. R. McKone, S. W. Boettcher, Q. X. Mi, E. A. Santori and N. S. Lewis, *Chem. Rev.*, 2010, **110**, 6446–6473.
 - 5 O. Khaselov and J. A. Turner, *Science*, 1998, **280**, 425–427.
 - 6 E. A. Hernandez-Pagan, N. M. Vargas-Barbosa, T. H. Wang, Y. X. Zhao, E. S. Smotkin and T. E. Mallouk, *Energy Environ. Sci.*, 2012, **5**, 7582–7589.
 - 7 A. Minguzzi, F. R. F. Fan, A. Vertova, S. Rondinini and A. J. Bard, *Chem. Sci.*, 2012, **3**, 217–229.
 - 8 J. F. Zhou, M. Unlu, J. A. Vega and P. A. Kohl, *J. Power Sources*, 2009, **190**, 285–292.
 - 9 G. Couture, A. Alaeddine, F. Boschet and B. Ameduri, *Prog. Polym. Sci.*, 2011, **36**, 1521–1557.
 - 10 A. Heller, H. J. Lewerenz and B. Miller, *J. Am. Chem. Soc.*, 1981, **103**, 200–201.
 - 11 A. Heller, B. Miller, H. J. Lewerenz and K. J. Bachmann, *J. Am. Chem. Soc.*, 1980, **102**, 6555–6556.
 - 12 J. R. McKone, A. P. Pieterick, H. B. Gray and N. S. Lewis, *J. Am. Chem. Soc.*, 2013, **135**, 223–231.
 - 13 S. Haussener, C. X. Xiang, J. M. Spurgeon, S. Ardo, N. S. Lewis and A. Z. Weber, *Energy Environ. Sci.*, 2012, **5**, 9922–9935.
 - 14 J. C. Hill and K. S. Choi, *J. Phys. Chem. C*, 2012, **116**, 7612–7620.
 - 15 X. Q. Chen, J. H. Ye, S. X. Ouyang, T. Kako, Z. S. Li and Z. G. Zou, *ACS Nano*, 2011, **5**, 4310–4318.
 - 16 J. K. Kim, K. Shin, S. M. Cho, T. W. Lee and J. H. Park, *Energy Environ. Sci.*, 2011, **4**, 1465–1470.
 - 17 F. M. Pesci, A. J. Cowan, B. D. Alexander, J. R. Durrant and D. R. Klug, *J. Phys. Chem. Lett.*, 2011, **2**, 1900–1903.
 - 18 R. Solarska, R. Jurczakowski and J. Augustynski, *Nanoscale*, 2012, **4**, 1553–1556.
 - 19 J. Z. Su, L. J. Guo, N. Z. Bao and C. A. Grimes, *Nano Lett.*, 2011, **11**, 1928–1933.
 - 20 B. D. Alexander, P. J. Kulesza, L. Rutkowska, R. Solarska and J. Augustynski, *J. Mater. Chem.*, 2008, **18**, 2298–2303.
 - 21 J. A. Seabold and K. S. Choi, *Chem. Mater.*, 2011, **23**, 1105–1112.
 - 22 R. Liu, Y. Lin, L. Y. Chou, S. W. Sheehan, W. He, F. Zhang, H. J. Hou and D. Wang, *Angew. Chem., Int. Ed.*, 2011, **50**, 499–502.
 - 23 V. Chakrapani, J. Thangala and M. K. Sunkara, *Int. J. Hydrogen Energy*, 2009, **34**, 9050–9059.
 - 24 W. Z. Li, J. Li, X. Wang, J. Ma and Q. Y. Chen, *Int. J. Hydrogen Energy*, 2010, **35**, 13137–13145.
 - 25 S. K. Deb, *Phys. Rev. B: Solid State*, 1977, **16**, 1020–1024.
 - 26 B. Cole, B. Marsen, E. Miller, Y. F. Yan, B. To, K. Jones and M. Al-Jassim, *J. Phys. Chem. C*, 2008, **112**, 5213–5220.
 - 27 Y. Y. Liu, Y. Li, W. Z. Li, S. Han and C. J. Liu, *Appl. Surf. Sci.*, 2012, **258**, 5038–5045.
 - 28 X. L. Sun, Z. M. Liu and H. T. Cao, *Thin Solid Films*, 2011, **519**, 3032–3036.
 - 29 R. Asahi, T. Morikawa, T. Ohwaki, K. Aoki and Y. Taga, *Science*, 2001, **293**, 269–271.
 - 30 M. Anik and T. Cansizoglu, *J. Appl. Electrochem.*, 2006, **36**, 603–608.
 - 31 R. S. Lillard, G. S. Kanner and D. P. Butt, *J. Electrochem. Soc.*, 1998, **145**, 2718–2725.
 - 32 R. Nakamura and Y. Nakato, *J. Am. Chem. Soc.*, 2004, **126**, 1290–1298.
 - 33 L. Weinhardt, M. Blum, M. Bar, C. Heske, B. Cole, B. Marsen and E. L. Miller, *J. Phys. Chem. C*, 2008, **112**, 3078–3082.
 - 34 G. M. Wang, Y. C. Ling, H. Y. Wang, X. Y. Yang, C. C. Wang, J. Z. Zhang and Y. Li, *Energy Environ. Sci.*, 2012, **5**, 6180–6187.
 - 35 Q. X. Mi, A. Zhanaidarova, B. S. Brunschwig, H. B. Gray and N. S. Lewis, *Energy Environ. Sci.*, 2012, **5**, 5694–5700.
 - 36 B. Marsen, B. Cole and E. L. Miller, *Sol. Energy Mater. Sol. Cells*, 2007, **91**, 1954–1958.
 - 37 L. Trotochaud, J. K. Ranney, K. N. Williams and S. W. Boettcher, *J. Am. Chem. Soc.*, 2012, **134**, 17253–17261.
 - 38 M. Yagi, E. Tomita and T. Kuwabara, *J. Electroanal. Chem.*, 2005, **579**, 83–88.
 - 39 Y. X. Zhao, E. A. Hernandez-Pagan, N. M. Vargas-Barbosa, J. L. Dysart and T. E. Mallouk, *J. Phys. Chem. Lett.*, 2011, **2**, 402–406.
 - 40 E. Narita, F. Lawson and K. N. Han, *Hydrometallurgy*, 1983, **10**, 21–37.
 - 41 A. J. Bard and L. R. Faulkner, *Electrochemical Methods: Fundamentals and Applications*, John Wiley & Sons, 2nd edn, 2001.
 - 42 L. Badia-Bou, E. Mas-Marza, P. Rodenas, E. M. Barea, F. Fabregat-Santiago, S. Gimenez, E. Peris and J. Bisquert, *J. Phys. Chem. C*, 2013, **117**, 3826–3833.
 - 43 M. Pourbaix, *Atlas of Electrochemical Equilibria in Aqueous Solution*, Pergamon Press, Oxford, 1966.
 - 44 B. Marsen, E. L. Miller, D. Paluselli and R. E. Rocheleau, *Int. J. Hydrogen Energy*, 2007, **32**, 3110–3115.
 - 45 L. Trotochaud, T. J. Mills and S. W. Boettcher, *J. Phys. Chem. Lett.*, 2013, **4**, 931–935.
 - 46 J. A. Seabold and K. S. Choi, *J. Am. Chem. Soc.*, 2012, **134**, 2186–2192.
 - 47 L. D. Burke and D. P. Whelan, *J. Electroanal. Chem.*, 1981, **124**, 333–337.
 - 48 C. C. Hu, Y. H. Huang and K. H. Chang, *J. Power Sources*, 2002, **108**, 117–127.
 - 49 R. C. Rossi, M. X. Tan and N. S. Lewis, *Appl. Phys. Lett.*, 2000, **77**, 2698–2700.